

Contents lists available at ScienceDirect

Tectonophysics

journal homepage: www.elsevier.com/locate/tecto





Evidence of crustal flexure induced by fluvial incisions

Felipe Baiadori ^{a,*}, Victor Sacek ^a, Bernardo T. Freitas ^b, Renato P. Almeida ^c

- a Instituto de Astronomia, Geofísica e Ciências Atmosféricas, Universidade de São Paulo, São Paulo, SP 05508-090, Brazil
- ^b Faculdade de Tecnologia, Universidade de Campinas, Limeira, SP 13484-332, Brazil
- c Instituto de Geociências, São Paulo, SP 05508-080, Brazil

ARTICLE INFO

Keywords: Numerical modelling Landscape evolution Tucano basin Flexural isostasy

ABSTRACT

Fluvial erosion of the Earth's crust creates valleys ranging from hundreds of meters to a few kilometers wide. The resulting unloading is supported by the flexural rigidity of the continental lithosphere. As a result, the bending of the lithosphere around individual river valleys is usually imperceptible in the landscape, specially in tectonically quiescent environments. However, in the Recôncavo-Tucano-Jatobá (RTJ) basins, an elongated Cretaceous rift located in northeastern Brazil, there is evidence of upward bending of sedimentary strata at the edges of the river valleys, where parts of the syn- and post-rift Late Cretaceous sedimentary layers were eroded. To assess whether the flexural response of the lithosphere due to fluvial erosion is able to explain the observed bending along the RTJ basins, we conducted a series of numerical experiments to evaluate the amplitude and wavelength of the lithospheric flexure achieved in the thermomechanical scenarios for the lithosphere, while imposing the observed amount of denudation derived from field data. We conclude that the wavelength and amplitude of the flexural behavior of the lithosphere obtained in the numerical scenarios are consistent with the observed bending only when the upper crust is partially decoupled from the lithospheric mantle, a configuration observed when the lower crust has a low effective viscosity. We propose that a combination of thermal and lithological factors contributed to induce the lithospheric decoupling, including heating of the lower crust due to magmatic underplating and the blanket effect created by the thick sedimentary layer preserved along the rift. Additionally, we propose that the flexural response of the lithosphere to individual river incisions is only noticeable in the continental lithosphere when the flexural rigidity of the lithosphere is low, with an effective elastic thickness (Te) ≲5 km.

1. Introduction

Vertical loads on the crust, such as sedimentary layers and orogenic wedges, are supported by the flexural rigidity of the lithosphere and the buoyancy forces exerted by the asthenosphere. This results in regional compensation with downward deflection of the lithospheric plate. The flexural behavior of the lithosphere is observed in the preservation of foreland basins and ocean trenches, as well as in the bending of the oceanic lithosphere around oceanic islands and seamounts (Watts, 2001; Allen and Allen, 2013). Conversely, the removal of mass through erosive exhumation causes unloading (negative load) of the crust and can induce a flexural response of the lithosphere in the opposite direction. This crustal unloading is evident in the formation of uplifted escarpments along divergent margins, where differential denudation of the margin, mainly along the coast, results in regional uplift. This contributes to preserving the altitude of the retreating escarpment (Gilchrist

and Summerfield, 1990; Kooi and Beaumont, 1994; Tucker and Slingerland, 1994).

The flexural response of the lithosphere depends on its flexural rigidity, as well as the dimensions and density of the vertical loads applied to the plate. River valley incisions that are hundreds of meters to a few kilometers wide are usually too narrow to induce a perceptible flexural response of the lithosphere. In this case, the rigidity of the plate supports the unloading caused by local erosion. On the other hand, geographically uniform erosion on a regional to continental scale results in uniform uplift of the lithosphere without significant internal bending. Therefore, the observation of lithospheric bending induced by erosion depends on the rigidity of the plate and the characteristic wavelength of the denudation.

Previous works have investigated the connection between river incision and the resulting mechanical response of the lithosphere mainly in active tectonic settings. For example, the studies by Garcia-

E-mail address: felipe.baiadori.silva@usp.br (F. Baiadori).

^{*} Corresponding author.

Castellanos (2002); Simpson (2004); Montgomery and Stolar (2006)

demonstrate that fluvial incisions can indeed have a significant impact on topography beyond valley excavation, as a result of the feedback between erosive and deep-lithospheric processes. However, the impact of river incisions in the cited works has been studied in a context of substantial simultaneous crustal shortening, and is largely associated with the intensification and concentration of background strain

resulting from tectonic activity. Simpson (2004) points out that the impact of rivers on the local strain pattern is primarily determined by the synchronous occurrence of river incision and regional deformation. The author also notes that without regional deformation, the erosion-induced response would have a significantly longer wavelength and would be too subtle to be discerned on the landscape.

In this study we present a novel example of flexural bending of the

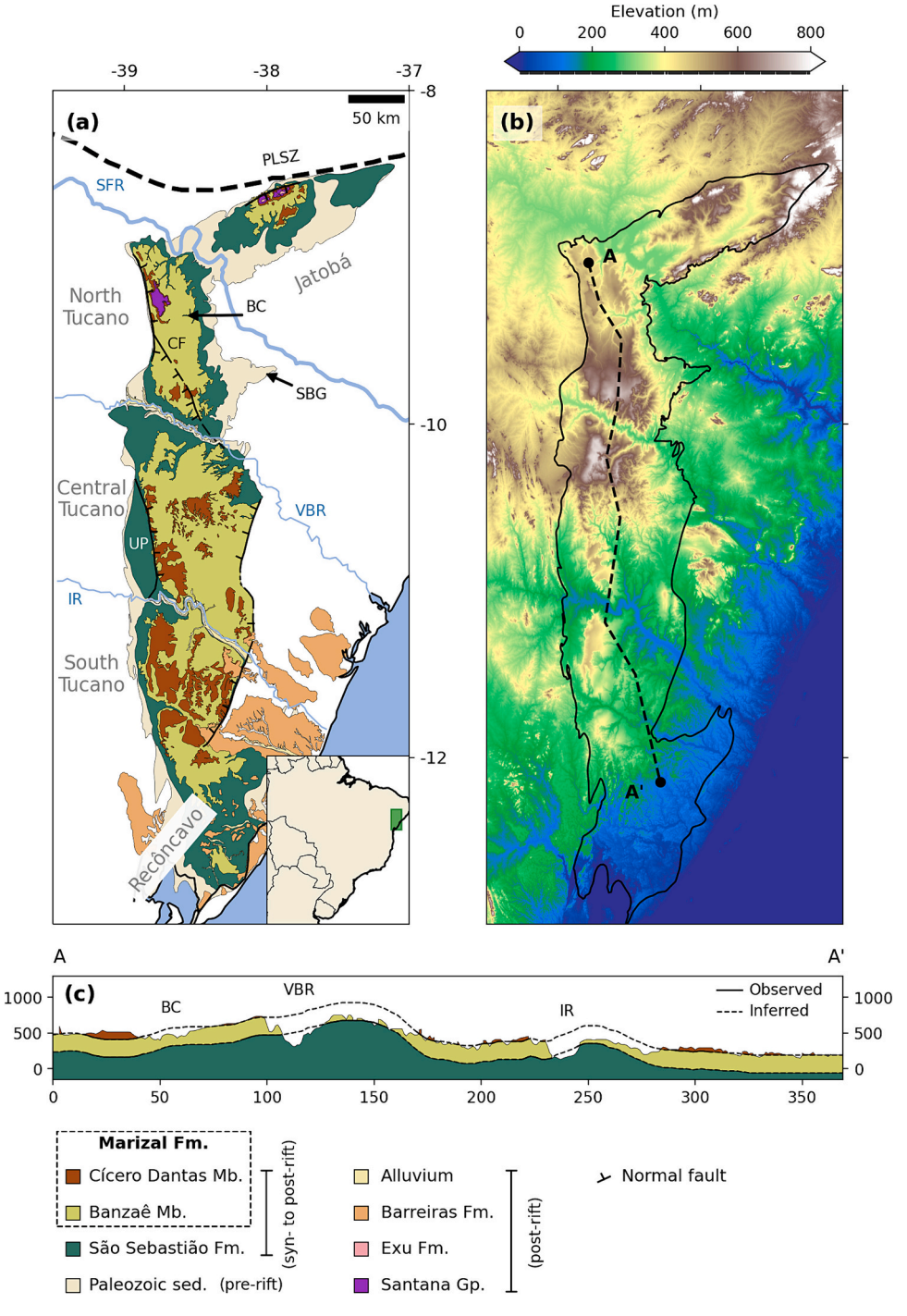


Fig. 1. (a) Geological map of the Recôncavo-Tucano-Jatobá intracontinental rift, emphasizing the distribution of the Aptian-aged sedimentary units comprising the Marizal Formation; (b) topographic map of the region, using data from the ETOPO 2022 digital elevation model (MacFerrin et al., 2022), and showing the location of the topographic profile used as constraint; (c) simplified geological profile showing the landscape and geometry of the sedimentary strata belonging to the São Sebastião and Marizal Formations. In panel c, black solid lines mark locations of observed contact between the Banzaê and Cícero Dantas members, whereas black dashed lines represent the inferred contact, drawn under the assumption of uniform thickness for the Banzaê Member. Panels a and c are both adapted from Freitas et al. (2017). SFR: São Francisco River; VBR: Vaza-Barris River; IR: Itapicuru River; BC: Baixa do Chico; SBG: Santa Brígida Graben; UP: Umburana Platform; CF: Caritá Fault; PLSZ: Pernambuco Lineament Shear Zone. Approximate location of PLSZ from Oliveira et al. (2023).

lithosphere induced by fluvial incisions in a tectonically quiescent environment. This process creates uplifted flanks at the borders of the valleys in the Recôncavo-Tucano-Jatobá (RTJ) basin system (Fig. 1a), an aborted rift in northeastern Brazil. Based on thermo-mechanical numerical simulations, we demonstrate that the low flexural rigidity along the RTJ rift, combined with localized fluvial incisions (Fig. 1b) in sedimentary rocks with varying degrees of erodibility, contributed to the creation of characteristic flexural patterns that are perceptible on the landscape (Fig. 1c). This observation provides important constraints on the rheology of the lithosphere beneath the RTJ rift during a period of relatively low tectonic activity, tens of millions of years after the end of the rifting phase.

2. Geological background

2.1. Structural and tectonic framework

The RTJ is an Early Cretaceous intracontinental rift located in the northeastern region of Brazil. It is comprised of three main connected sedimentary basins: Recôncavo, Tucano, and Jatobá basins. The genesis of the rift is related to the Camamu-Almada and Jacuípe offshore basins, and it is interpreted as a failed branch of the South Atlantic rift, associated with the Gondwana break-up event (Matos, 1992; Gordon et al., 2017).

Its general orientation is approximately north-south, with an axial length of about 400 km, and a maximum width of no more than 100 km. Near its northern boundary, there is a shift in the rift trend to ENE-WSW (Fig. 1a), which is likely influenced by the presence of the Pernambuco Shear Zone (Gordon et al., 2017). This rift system crosses the boundary between the Borborema (to the north) and São Francisco (to the south) tectonic provinces, each with markedly distinct structural frameworks. This complex structural inheritance is believed to have played a significant role in the formation of the RTJ, influencing the formation of the faults that characterize the basin system's architecture.

One of the most remarkable aspects concerning the basement structure of the rift is the shift in dip polarity between consecutive half-grabens (Milani and Davison, 1988): to the south of the Vaza-Barris transfer zone, the border fault of the Recôncavo, South and Central Tucano sub-basins is located to the east of the depocenter, whereas to the north of the transfer zone, the border fault is situated to the west. This feature is often regarded as an example of how preexisting structures related to the Pan-African/Brasiliano orogeny have influenced the architecture of the RTJ rift (Magnavita and Cupertino, 1988). Moreover, equally remarkable are the great sedimentary thicknesses preserved in the depocenters of the Tucano basin, particularly in the Central Tucano, where basement depths have been estimated to reach over 16 km in the Cícero Dantas Low (Costa et al., 2007; Alvarez and Holz, 2022), while in the rest of the system, basement depths typically range between 5 and 8 km (Aragão and Peraro, 1994; Freitas et al., 2017).

2.2. Rift stratigraphy

Sedimentary strata in the RTJ exhibit ages spanning from the Paleozoic to the Cenozoic. Observations indicate that the thickness of the Paleozoic units is greater in the Santa Brígida graben, close to the North Tucano and Jatobá sub-basins. Caixeta et al. (1994) provides an account of the different depositional environments associated with the Paleozoic section.

The pre-rift section corresponds to the Late Jurassic Brotas Group (Aliança and Sergi Formations), Itaparica and Água Grande Formations. These units consist mainly of red beds of continental origin, which are associated with alternating fluvial-eolian cycles and lacustrine transgressions. The sedimentary thicknesses exhibit significant variability along the rift axis (Costa et al., 2007). Although some studies (Magnavita and Cupertino, 1988; Milani and Davison, 1988) indicate that rifting began at the base of the fanglomerates deposited close to the border

faults, the onset of the rifting stage is more commonly associated with the deposition of the Candeias lacustrine units over the fluvial-eolian pre-rift units. This is believed to signal both an increase in subsidence rates due to crustal faulting and a shift from and arid to a more humid climate (Caixeta et al., 1994; Silva et al., 2007, and references therein). Accordingly, this work considers the beginning of the *syn*-rift stage to be marked by the deposition of the Candeias sediments.

Overall, the syn-rift section consists largely of continental sediments that record significant variations in the generation of accommodation space to sediment input ratio. Beginning in a sediment-starved, lacustrine setting developed in response to the initial tectonic subsidence, sediment supply later surpassed accommodation. Increasing sedimentation rates led to gradual infilling by gravity flows, deltaic sediments, and fluvial deposits. The final stages of rift activity are commonly associated in the literature to the São Sebastião Formation (Costa et al., 2007), which is exposed in several localities within the RTJ (Fig. 1a). This succession consists mainly of quartz-rich pebbly sandstone of fluvial origin, with occasional occurrences of mudstone and heterolithic strata, as well as vein quartz-dominated conglomerate composition (Figueiredo et al., 2016).

The Aptian sedimentary units of the RTJ, mainly referred to as Marizal Formation, are separated from the São Sebastião deposits by an angular unconformity and exposed throughout much of the basin system, particularly in the Tucano and Jatobá basins (Fig. 1a). The Marizal Formation is often interpreted as the sedimentary response to a rather subdued post-rift thermal subsidence phase (Costa et al., 2007; Magnavita and Cupertino, 1988). Figueiredo et al. (2016) investigated the causes for the observed reduction in sandstone and conglomerate maturity from the São Sebastião (quartz-rich) to the Marizal (feldsparrich) formations in the Tucano basin, by performing provenance analysis of the gravel fraction in these units and correlatable deposits. Their results show a marked change in the configuration of the source area, indicating a model that involves border fault reactivation subsequent to erosional retreat of rift flanks during deposition of the Marizal Formation.

The Marizal Formation was later subdivided into the clastic-dominated lower Banzaê and upper Cícero Dantas members, first described in Freitas et al. (2017) as showing contrasting fluvial architectures, and being locally separated by the fossiliferous Amargosa Bed. The thickness of the Banzaê Member is approximately 250 m where fully preserved, while the Cícero Dantas Member reaches up to 150 m. In the same work, the authors verified local faulting within these strata, suggesting that the active tectonic stage of the RTJ may have extended through the Aptian, supporting the findings of Figueiredo et al. (2016). This interpretation is supported by the analysis of shear band structures concentrated in the Vaza-Barris transfer zone, reported in Gomes et al. (2018), which reveals a well distributed presence of these subseismic-scale structures, reflecting continuous regional extension even during deposition of the Banzaê Member.

In certain areas of the North Tucano and Jatobá grabens, the Marizal sediments are observed to be covered by post-rift carbonate-bearing successions that are correlated with the Santana Group of the Araripe basin, located approximately 200 km northwest of the RTJ (Freitas et al., 2017). These successions are interpreted as the remaining portions of regional lacustrine carbonate deposits from the Aptian in association with a rise in base level, possibly connecting several basins in the Brazilian northeast (Varejão et al., 2016). Furthermore, the carbonate successions in the Jatobá basin are locally overlain by non-fossiliferous coarse to conglomeratic sandstones belonging to the Albian-aged Exu Formation, which is believed to have deposited in a fluvial braided to meandering environment (Neumann and Rocha, 2014).

2.3. Post-rift evolution

Since the deposition of the Marizal Formation in the Cretaceous period, the sea level dropped nearly 200 m (Haq, 2014), leading to the

formation of topographic relief due to base level fall. Additionally, the topographic relief was probably amplified by magmatic underplating, as proposed by Magnavita et al. (1994). Following these events, the surrounding domains of the RTJ system were continuously eroded, resulting in regional uplift while the sedimentary layers of the Banzaê Member were preserved due to resistance to erosion (Gomes et al., 2018).

These sedimentary strata resistant to erosion along the RTJ system were segmented by individual fluvial incisions (namely, the São Francisco, Vaza-Barris and Itapicuru rivers, Fig. 1a), creating a complex three-dimensional morphology (Fig. 1b). At the borders of the river valleys, especially along the Vaza-Barris and Itapicuru rivers, it is possible to observe uplifted flanks with short wavelength, comparable to the width of the basin system, across a few tens of kilometers (Fig. 1c). They are roughly symmetrical in terms of elevation with respect to the Vaza-Barris and Itapicuru incisions (Fig. 1c), and coincide with areas where the Banzaê Member of the Marizal Formation is well preserved.

Some deep-rooted, *syn*-tectonic structures, such as the Caritá fault and the Umburana Platform eastern fault, hold spatial relations to the uplifted Vaza-Barris flanks. The Caritá fault crosses the northern flank, as may be noted in Fig. 1a, but it exhibits minor topographic expression. Close to the western border of the Central Tucano, the Umburana Platform fault appears to limit the occurrence of the Marizal sediments, though its influence on the magnitude of the adjacent uplift seems to be only secondary. From these observations, one might infer that the elevation of river incision flanks in the RTJ is only weakly, if at all, controlled by the activity of syn-rift structures. Therefore, it may well have originated during the post-rift phase of the basin system. This inference is reinforced by the strong correlation between the borders of elevated terrains and the drainage pattern within the basin. This indicates that a possible mechanism for the uplift of the river valleys is due to flexural response to sediment removal along the fluvial incisions.

Alternatively, Freitas et al. (2017) suggested that differential compaction may have been responsible for the observed curvature of the Aptian strata, based on the position of the synform of these layers roughly over rift depocenters. However, upon closer inspection, the position and orientation of the antiforms and synforms axes show a remarkable shift from the asymmetrical distribution of depocenters along the Tucano basin. Moreover, the uniformity of the thickness of the Banzaê layer throughout most of the RTJ system and the close match between stratal antiforms and main river flanks favor the hypothesis that the deformation of Aptian units might be primarily due to flexural uplift in the vicinity of modern river valleys.

3. Methods

To test the hypothesis of the flexural origin of uplifted flanks at the borders of river valleys along the RTJ rift, we developed numerical scenarios to evaluate the influence of fluvial incisions on the stress and strain rate patterns in the lithosphere.

3.1. Model equations

The present work utilizes the finite element thermomechanical software Mandyoc (Sacek et al., 2022), suitable for simulating different geodynamic problems related to lithosphere dynamics (e.g. Silva and Sacek, 2022; Salazar-Mora and Sacek, 2023; Silva et al., 2023). Mandyoc solves the equations for conservation of mass, momentum, and energy for incompressible viscous flow:

$$\nabla \cdot \mathbf{u} = 0 \tag{1}$$

$$\nabla \cdot \boldsymbol{\sigma} + \rho \mathbf{g} = 0 \tag{2}$$

$$\frac{\partial T}{\partial t} + \mathbf{u} \cdot \nabla T = \nabla \cdot (\kappa \nabla T) + \frac{H}{c_n} + \frac{\mathbf{u} \cdot \mathbf{g} \alpha T}{c_n}$$
(3)

where

$$\sigma = -P\mathbf{I} + \eta(\nabla \mathbf{u} + \nabla^{\mathsf{T}} \mathbf{u}) \tag{4}$$

$$\rho(T) = \rho_0 [1 - \alpha (T - T_0)], \tag{5}$$

u represents the velocity vector, **g** is the gravity acceleration, T is the temperature, t is the time variable, κ is the thermal diffusivity, ρ is the effective density for mantle rocks, ρ_0 is the reference density at temperature $T=T_0=0^{\circ}\mathrm{C}$, H is the radiogenic heat production per unit mass, c_p is the specific heat capacity at constant pressure, P is the total pressure, P is the effective rock viscosity, and P is the identity matrix.

Deformation within the modeled lithospheric and asthenospheric rocks is calculated by assuming a combination of viscous and plastic rheologies. Viscous deformation is controlled by the following nonlinear power law that relates the ductile viscosity to temperature, pressure, and strain rate:

$$\eta_{\text{duct}} = C \cdot A^{-\frac{1}{n}} \dot{\varepsilon}_{n}^{\frac{1-n}{n}} \cdot \exp\left(\frac{Q + VP}{nRT}\right)$$
 (6)

where *A* is a pre-exponential factor, *n* is the exponent of the power law, $\frac{1}{2}$

$$\dot{arepsilon}_{II}=\left(\dot{arepsilon}_{ij}\dot{arepsilon}_{ij}/2
ight)^{1/2}$$
 is the second invariant of the strain rate tensor, Q and

V are, respectively, the activation energy and volume for viscous creep, P and T are the pressure and temperature, R is the universal gas constant, and C is a compositional factor introduced in Sacek (2017) to scale the viscosity, providing a way to easily vary the degree of coupling of the lithosphere (smaller values of C for the lower crust imply a "more weakly" coupled lithosphere). The values for A, D, D and D for olivine and quartz are extracted from Karato and Wu (1993) and Gleason and Tullis (1995), respectively, and shown in Table 1.

Plastic deformation is simulated in the thermomechanical code using the Drucker-Prager criterion:

$$\sigma_{\text{vield}} = c_0 \cdot \cos\phi + P \cdot \sin\phi \tag{7}$$

where ϕ is the angle of internal friction and c_0 is a coefficient which reflects the internal cohesion of the rock. The effective viscosity is thus determined from both the viscous and plastic components as (Moresi and Solomatov, 1998):

$$\eta = min(\eta_{\text{plast}}, \eta_{\text{duct}}) = min\left(\frac{\sigma_{\text{yield}}}{2\dot{\varepsilon}_{II}}, \eta_{\text{duct}}\right). \tag{8}$$

Table 1

Physical and rheological parameters for each layer in the simulations. Values extracted from Karato and Wu (1993) for olivine and from Gleason and Tullis (1995) for quartz. DO = dry olivine; WO = wet olivine; numerical values for referred constants are: $A_{\rm air}=1.0\times10^{-18},\ A_{\rm quartz}=8.574\times10^{-28},\ A_{\rm DO}=2.4168\times10^{-15},\ A_{\rm WO}=1.393\times10^{-14},\ H_{\rm uc}=9.26\times10^{-10},\ {\rm and}\ H_{\rm lc}=2.86\times10^{-10}.$

	Air	Sediment	Upper crust	Lower crust	Litho. mantle	Asthenos.
Reference density (kg.m ⁻³)	1	2500	2700	2800	3354	3378
Creep flow law	-	Quartz	Quartz	Quartz	Dry olivine	Wet olivine
$A (Pa^{-n}/s)$	$A_{\rm air}$	$A_{ m quartz}$	$A_{ m quartz}$	$A_{ m quartz}$	$A_{ m DO}$	$A_{ m WO}$
Q (kJ/mol)	0	222	222	222	540	429
n	1	4	4	4	3.5	3
$V (m^3/\text{mol})$	0	0	0	0	$25 \times$	15×
					10^{-6}	10^{-6}
H (W/kg)	0	$H_{ m uc}$	$H_{ m uc}$	H_{lc}	9 ×	0
					10^{-12}	
$\kappa (\mathrm{m}^2/\mathrm{s})$	1 ×	5×10^{-7}	1 ×	1 ×	1 ×	1×10^{-6}
	10^{-6}		10^{-6}	10^{-6}	10^{-6}	

F. Baiadori et al. Tectonophysics 877 (2024) 230292

3.2. Numerical Setup

The adopted setup has horizontal and vertical dimensions of 1600 km and 300 km, respectively, subdivided in $1 \times 1 \text{ km}^2$ elements. The thickness of the lithosphere is set to be 100 km, including the sedimentary layer, upper crust, lower crust, and the lithospheric mantle (Fig. 2). The value used for crustal thickness is based on Döring et al. (2022). Interfaces between layers beneath the surface are all assumed to be initially horizontal. This assumption is partly made because, although variations in upper crustal thickness in the study region are recognized, these features were likely already isostatically compensated by the end of the rifting period and, thus, bear little relevance to the evolution of the basin system during the post-rift period.

The initial thermal structure of the model lithosphere is only depth dependent, and corresponds to the solution of the following equation:

$$0 = \frac{\partial}{\partial z} \left(\kappa \frac{\partial T}{\partial z} \right) + \frac{H(z)}{c_p} \tag{9}$$

where H is the radiogenic heat production. As boundary conditions for Eq. (9), the temperature at the surface and at the base of the lithosphere are fixed at 0°C and 1300°C, respectively. This form of the heat equation accounts for vertical variations in the thermal conductivity (and, hence, diffusivity κ) of the rocks, thus allowing us to simulate the effect of thermal blanketing by sediments with lower conductivity on the temperature field. The insertion of a less conductive sedimentary layer, together with the radiogenic source term, affects the steady-state thermal profile by preserving higher subsurface temperature gradient (Fig. 2).

Initial temperatures in the sublithospheric mantle increase adiabatically with depth, and are described by the expression:

$$T(z) = T_p \cdot exp(g\alpha z/c_p) \tag{10}$$

where $T_p=1262^{\circ}\mathrm{C}$ is the potential temperature for the mantle. Boundary conditions for the temperature field throughout the simulation are such that the temperature values on the lateral boundaries of the model domain are free, while keeping the temperature on the top and bottom boundaries fixed.

The initial topography assumes that the stratigraphic layers are horizontal, therefore representing the geometry of the layers before any flexural bending has occurred. At the top of the free surface, erosion is

imposed based on the profile from Freitas et al. (2017). It is assumed that the total thickness of eroded sedimentary rock can be determined by the difference between the actual topography and the envelope indicated by the dashed line in Fig. 1d, resulting in the initial topography as shown in Fig. 2. The initial curve is positioned near the center of the numerical domain, and the horizontal extent of the model domain (1600 km) is kept much greater than the total length of the profile (\sim 370 km). This setup helps prevent buondary effects from affecting the numerical simulation.

Our 2D models cannot directly reproduce the 3D denudation pattern around the uplifted Late Cretaceous sedimentary rocks in the RTJ basins (Fig. 1c), especially the denudation over the Vaza-Barris and Itapicuru drainage basin area. This is because data on the geometry of the Aptian strata in areas adjacent to the geologic profile are more scarce. Since these data are essential in constraining the amount of denudation and uplift, the lack of sufficient information regarding stratal geometries in off-profile regions hinders a three-dimensional approach to the problem. Instead, to account for the impact of unloading in these regions, we introduced compensation zones (Fig. 2) in certain numerical scenarios. Two of these zones can be identified on the geologic map (Fig. 1a) as areas of significant exposure of the São Sebastião Formation, such as observed west of the Vaza-Barris and Itapicuru river valleys. The third zone of compensation includes the effect of denudation occurring to the east of the Baixa do Chico area, north of the Vaza-Barris, as a consequence of a significant fluvial incision that flows into the São Francisco River farther east.

In the compensation zones, three-dimensional removal of surface material is represented by a local decrease in sediment density. This density contrast between the zones and the surrounding sediment is calculated as follows: given the thickness $h_{\rm off}$ of off-profile denudated material and the depth of compensation $d_{\rm comp}$, the decrease $\Delta \rho$ in the density is

$$\Delta \rho g d_{\text{comp}} = \rho_{\text{sed}} g h_{\text{off}} \rightarrow \Delta \rho = \frac{\rho_{\text{sed}} h_{\text{off}}}{d_{\text{comp}}}$$
(11)

where $\rho_{\rm sed}$ is the density assumed for the sedimentary layer. Taking $\rho_{\rm sed}=2500~{\rm kg.m}^{-3},~h_{\rm off}=330~{\rm m}$ (corresponding to the combined thicknesses of the Banzaê and Cícero Dantas Members), and $d_{\rm comp}=5~{\rm km}$, one obtains $\Delta\rho=165~{\rm kg.m}^{-3}$, yielding a value of $\rho_{\rm comp}=2335~{\rm kg.m}^{-3}$ for the compensation zones. The value for $h_{\rm off}=330~{\rm m}$ represents a lower limit, assuming that the exhumation removed only the Banzaê and

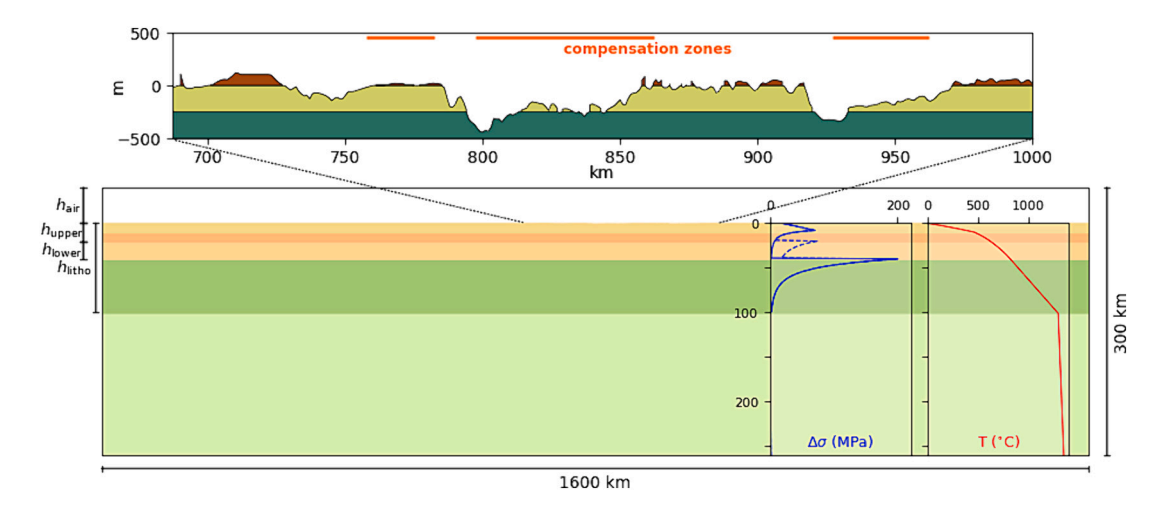


Fig. 2. Numerical setup adopted for the simulations. The thicknesses of the air, upper and lower crustal layers are, respectively: $h_{\rm air} = 40$ km, $h_{\rm upper} = h_{\rm sed} + h_{\rm base} = 20$ km, and $h_{\rm lower} = 20$ km, where $h_{\rm sed} = h_{\rm base} = 10$ km are the respective thicknesses of the sediment fill and upper crustal basement. The total thickness of the lithosphere $h_{\rm litho} = 100$ km. The upper panel shows the initial topographic curve between 687 km and 1000 km. Blue curves show the yield strength envelope for the cases where C = 1 (solid curve) and C = 10 (dashed curve), assuming $\dot{\varepsilon}_{II} = 10^{-14}$ s⁻¹, $c_0 = 20$ MPa, and $\phi = 15^{\circ}$; red curve corresponds to the initial thermal profile, and orange horizontal lines in the upper panel indicate the lateral extent of the compensation zones (see text) projected on the profile. (For interpretation of the references to colour in this figure legend, the reader is referred to the web version of this article.)

Cícero Dantas members (Fig. 1c), exposing the top of the São Sebastião Formation without additional erosion of this formation. The choice of d_{comp} is arbitrary and must be chosen so that the product $d_{\text{comp}} \cdot \Delta \rho$ is the same, resulting in the same unloading effect.

4. Modelling results

4.1. Reference models

The scenarios used as comparative references to subsequent simulations feature the setup shown in Fig. 2, and differ only in the value assumed for the compositional scaling factor C for the lower crust: C=10 for the first reference scenario, and C=1 for the second reference scenario. For the same temperature, pressure, and strain rate conditions, the lower crust in the first reference scenario (C=10) is ten times more viscous than in the second reference scenario (C=1). Consequently, the first reference scenario exhibits a higher degree of mechanical coupling between the crust and lithospheric mantle compared to the second reference scenario. In both reference scenarios, only the unloading indicated by the erosion along the 2D profile is considered.

The change in lower crustal rheology, which modifies the degree of coupling in the lithosphere, had a profound impact on the strain pattern in the crust and mantle (Fig. 3): the strain pattern resulting from the first reference simulation is characterized by significant amounts of strain affecting the crust and lithospheric mantle, and a widespread sublithospheric zone whereby most of the deformation takes place, with asthenospheric flow inducing the buoyancy forces beneath the lithosphere (Fig. 3a). In contrast, the strain pattern in the second reference scenario is marked by a highly strained region within the crust (Fig. 3c), with lower strain magnitudes in the lithospheric mantle. The difference between the simulated deformation patterns in both reference scenarios is manifested on the surface as different topographic curves (Fig. 3b,d): The resultant topography from the first simulation is more subdued, characterized by low-relief, longer-wavelength features and low curvature of the strata. On the other hand, topographic features in the second simulation show shorter wavelength, more accentuated relief and visible curvature of the strata. The contrast between the strain distribution and

topographic forms of the reference scenarios can be explained by considering that lower values of *C* for the lower crust imply a less efficient transmission of stresses to greater depths, promoting strain localization in the lower crust.

4.2. Models including off-profile loads

A second set of simulations takes into account additional flexural loads resulting from the removal of material from nearby off-profile regions by incorporating artificial compensation zones within the sediment layer. The lateral extents of these zones are selected to be roughly equivalent to those of the adjacent significantly exhumed areas. A result of this approach is, as expected, the amplification of the total uplift at points close to or on the compensation zones (Fig. 4).

Thus, with respect to the reference scenarios (Fig. 4b,c), the topographic curves resulting from simulations with zones of compensation within the sediment layer show more pronounced relief (Fig. 4d). Moreover, in scenarios considering off-profile denudation, the amount of modeled uplift over the flanks of incised valleys creates a topographic form and curvature that align more coherently with observations (Fig. 4e) compared to those resulting from reference scenarios.

4.3. Degree of lithospheric coupling

Although the distribution of surface loads is of primary importance, the degree of coupling of the lithosphere, as expressed by the value of the viscosity scaling factor *C* for the lower crust, also exerts a major influence on the final topographic geometry. This occurs because the rheological behavior of lower crustal rocks determines the depth at which stresses associated with loads applied on the surface are balanced, consequently controlling the effective elastic thickness of the lithosphere and the resulting uplift pattern (Burov and Diament, 1995).

In light of this, several simulations were run, differing only in the scaling factor C for the lower crust, with the purpose of investigating which value of this parameter provides an adequate fit for the actual topography. This evaluation is conducted using the concept of cosine similarity between two vectors \mathbf{x} and \mathbf{y} , defined as:

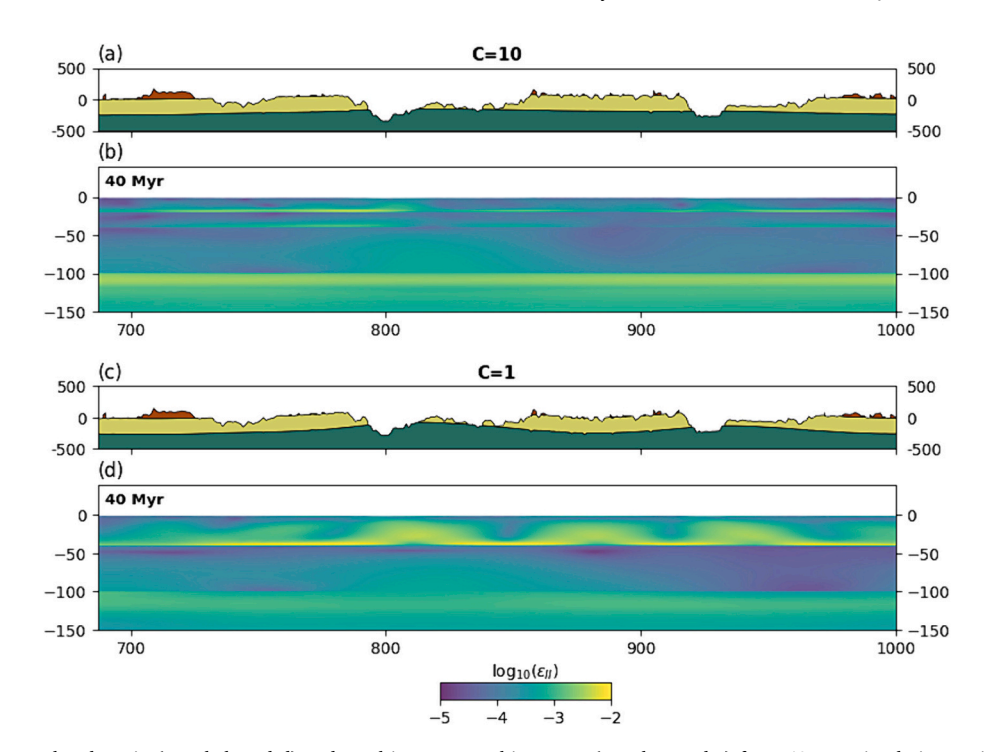


Fig. 3. Patterns of accummulated strain (panels b and d) and resulting topographic curves (panels a and c) for a 40 Myr simulation period in the reference simulations with C = 10 and C = 1 for the lower crust. Topographic profiles are coloured to represent sedimentary strata in accordance with Freitas et al. (2017).

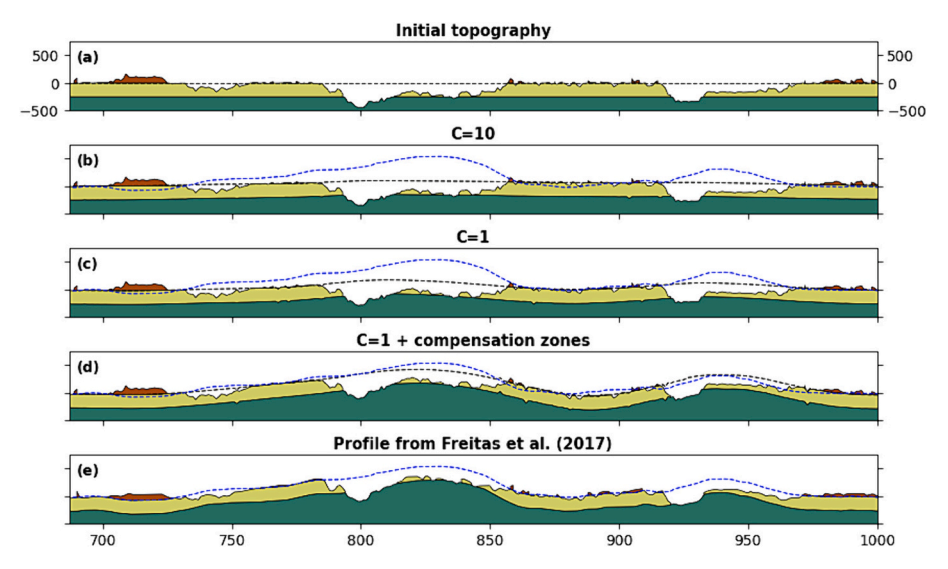


Fig. 4. (a) Initial model topography and envelope (black dashed curve); (b-c) topographic and envelope curves resulting from the reference simulations; (d) final curves for a scenario accounting for off-profile denudation with C = 1 for the lower crust; (e) Geologic profile and erosive envelope from Freitas et al. (2017), reduced of the regional component. The observed erosive envelope (blue dashed curve) is plotted in panels b-d for comparison. (For interpretation of the references to colour in this figure legend, the reader is referred to the web version of this article.)

$$S_{\cos}(\mathbf{x}, \mathbf{y}) = \frac{\mathbf{x} \cdot \mathbf{y}}{|\mathbf{x}||\mathbf{y}|}.$$
 (12)

Eq. (12) expresses the cosine of the angle between two vectors with any number of components, thus it only takes values in the range of -1 to 1. It is to be interpreted in the following manner: values closer to 1 imply that the input vectors have more similar directions, and, thus, are more closely aligned. When the input vectors correspond to the observed and modeled uplift curves, the cosine similarity provides a measure of the "likeness" between these curves, and can be used to determine which model best fits the constraints, i.e., the one that maximizes the similarity. It must be mentioned that cosine similarity is usually employed in circumstances where the magnitude of the input vectors (here represented by the uplift amplitude) is less important than their respective directions (here controlled by the lateral distribution of the uplift).

The adopted criterion allows us to note some aspects, as illustrated in Fig. 5. Firstly, high values of C are associated with a low similarity, due to lower amplitudes of the simulated maximum uplift, as well as longer wavelengths in comparison to the observed curve. A second noteworthy point is that, for C > 2, the similarity starts to decrease dramatically, while for C between 0.1 and 2 the similarity shows little variation, being maximized for C = 1. This is mostly due to the fact that wavelength values for the uplift in scenarios with the lowest degrees of coupling (0.1, 1, 2) do not differ significantly among them.

The maximum uplift has been observed to be greater in scenarios where coupling between the upper crust and the lithospheric mantle is

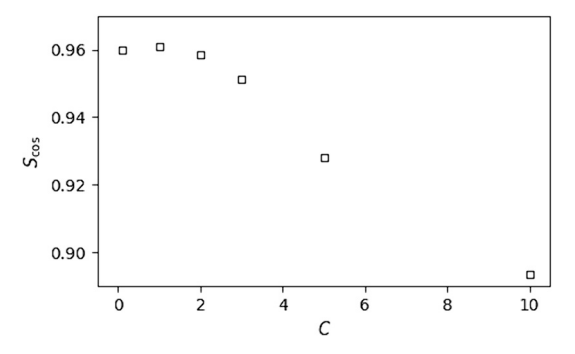


Fig. 5. Cosine similarity as a function of the viscosity scaling factor C for the lower crust.

weaker. Up to 75% of the maximum observed uplift is reproduced in these models. In these scenarios, uplift is also less distributed laterally, being largely concentrated near the incised valleys. This reflects the accommodation of isostatically imposed stresses through viscous flow of material in lower crustal depths.

5. Discussion

5.1. Rheological implications

Our numerical results indicate that the bending of the Cretaceous sedimentary layers along the RTJ rift can be explained by the flexural response of the upper crust to the post-rift denudation along the fluvial incisions of the Itapicuru and Vaza-Barris Rivers. Only scenarios with a low degree of lithospheric coupling were able to reproduce both the relatively short wavelength and high amplitude of the flexural uplift.

At this point, it is worth stressing that due to immediate removal of surface material at the beginning of our simulations, strain rate magnitudes across the model domain during the first few million years are expressively higher than they would be if the removal was distributed over time (i.e., incorporating finite rates of denudation). The ductile viscosity (and, hence, the effective viscosity) of the lower crust shows a significant nonlinear dependence on the magnitudes of strain rates. In particular, as shown in Burov and Diament (1995), the yield strength of the lithosphere is significantly enhanced by higher strain rates, implying that, in the simulations presented here, the value obtained for lower crustal C may be somewhat lower than what would be estimated in scenarios including surface processes at finite rates. This has no bearing on the result that the presence of observed landforms in the studied region requires a low degree of lithospheric coupling. Thus, we speculate that the incorporation of time-distributed erosion into the simulations would not significantly increase the estimated value of C for the

The decoupled state of the lithosphere along the RTJ rift, resulting from a low-viscosity lower crust, may be attributed to either lithological or thermal factors. Evidence for thermal perturbation in the form of magmatic underplating, as proposed by Magnavita et al. (1994), is also supported by Alvarez and Holz (2022) and Döring et al. (2022). To quantify the thermal influence of the magmatic underplating, we used the analytical solution to the one-dimensional, unsteady heat conduction of an infinite region (Turcotte and Schubert, 2002):

$$T = T_0 + \frac{Q}{2\rho c \sqrt{\pi \kappa t}} e^{-z^2/4\kappa t} \tag{13}$$

where Q is the heat content of the magmatic underplating per unit area given by

$$Q = \rho[c(T_u - T_0) + L]h_u \tag{14}$$

and T_u is the temperature of the magma, T_0 is the temperature of the country rock, ρ is the rock density, c is the specific heat capacity, L is the latent heat of fusion, and h_u is the thickness of the magmatic underplating. Assuming h_u is between 3.5 and 5 km (Alvarez and Holz, 2022) with $T_u - T_0 = 500 \text{ K}$, $\rho = 2800 \text{ kg/m}^3$, $c = 1.2 \text{ kJ kg}^{-1} \text{ K}^{-1}$, L = 320 kJkg⁻¹, and $\kappa = 1.0 \times 10^{-6}$ m²/s, the thermal perturbation $T - T_0$ is smaller than 100 K after 1.8 and 3.7 Myr, respectively, and continues to cool down over time. Therefore, the thermal perturbation induced by magmatic underplating endures for only a few million years, representing a transient thermal disturbance that temporarily weakens the lower crust. However, if part of the magmatic underplating occurred during the post-rift phase, as suggested by Magnavita et al. (1994) and discussed by Döring et al. (2022), this magmatic event contributed to inducing regional uplift concomitant with the thermal weakening of the lower crust. In this scenario, it is plausible that the largest denudation (unloading) rate along the RTJ Basins occurred when the lower crust was weaker due to the heat of the underplating magmatic event.

Alternatively, the thick sedimentary layer with lower thermal conductivity than the crystalline rocks could contribute to permanent heating of the crust and lithospheric mantle due to the blanket effect, leading to the induction of lithospheric decoupling (e.g. Lavier and Steckler, 1997). However, assuming that the sedimentary layer is 10 km thick with a thermal diffusivity κ_s equal to half that of the crystalline rock ($\kappa_s = \kappa/2$), the maximum temperature increase at the base of the crust is less than 70 K after a few tens of million years. This estimate was calculated based on a simple analytical model assuming two layers with different thermal diffusivity. Therefore, the blanket effect has a modest contribution to weakening the lower crust to induce lithospheric decoupling.

Another plausible mechanism for inducing permanent lithospheric decoupling is lithological. This explains the low compositional factor (\mathcal{C}) in our numerical scenarios, which is necessary to elucidate the observed flexural behavior in the post-rift phase of the RTJ Basins. We speculate that the underplating at the base of the crust could contribute to creating metasomatic influence on the lower crust, affecting its effective viscosity.

5.2. Analysis of the flexural rigidity of the lithosphere in the RTJ basins

The short wavelength obtained in our thermo-mechanical numerical models is compatible with the low effective elastic thickness T_e estimated by Magnavita et al. (1994) for the rifting phase: $T_e=5$ km. This agreement is explained by considering that, even though the shortwavelength uplift is observed in the present topography, the current configuration of the Vaza-Barris and Itapicuru rivers has not necessarily been established recently, and denudation has acted continuosly during the post-rift period. In other words: although the flexural bending of the Aptian layers occurred in the post-rift phase, it is not necessarily recent.

Based on the simple thin elastic plate approach, the vertical deflection w of the plate under a periodic load with wavelength λ_f and amplitude h is given by (Watts, 2001):

$$w = \left(\frac{\rho_c - \rho_i}{\rho_m - \rho_i}\right) h\cos(2\pi x/\lambda_f)\phi_e(\lambda_f)$$
(15)

where ρ_c is the density of the crust, ρ_m is the density of the mantle, ρ_i is the density of the material displaced at the surface, and ϕ_e is the flexural response function given by

$$\phi_e(\lambda_f) = \left[\frac{D\left(\frac{2\pi}{\lambda_f}\right)^4}{(\rho_m - \rho_i)g} + 1 \right]^{-1}$$
(16)

where D is the flexural rigidity of the plate and g is the gravity acceleration. The flexural rigidity D can be rewritten as function of the effective elastic thickness T_e :

$$D = \frac{ET_e^3}{12(1 - \nu^2)} \tag{17}$$

where *E* is the Young's modulus and ν is the Poisson's ratio. From Eq. (15), the maximum curvature of the plate is

$$K \equiv max \left| \frac{d^2w}{dx^2} \right| = \left(\frac{\rho_c - \rho_i}{\rho_m - \rho_i} \right) \frac{4\pi^2 h}{\lambda_f^2} \phi_e(\lambda_f)$$
 (18)

Assuming that the peak-to-peak amplitude is 2h = 400 m, compatible with the post-rift denudation along the RTJ rift, with $\rho_c=2700~{\rm kg/}$ m^3 and $\rho_i = 0$ (air), the maximum curvature K for unloading with wavelength $\lambda_f = 30-80$ km (similar to the valley width along the Itapicurú and Vaza-Barris Rivers) obtained for $T_e = 5$ km is between K = $1-5\times10^{-7}~\text{m}^{-1}$ (yellow region in Fig. 6b). On the other hand, the maximum plate curvature for $T_e=12\,\mathrm{km}$ is $<6\times10^{-8}\,\mathrm{m}^{-1}$ and for $T_e=12\,\mathrm{km}$ 25 km is $< 1 \times 10^{-8}$ m⁻¹ in the same λ_f interval (Fig. 6b). Plate curvature on the order of 10^{-8} m⁻¹, which corresponds to a radius of curvature R = 10^5 km (assuming $K \approx 1/R$), is approximately one order of magnitude smaller than the curvature of Earth itself ($K_{Earth} \approx 1.56 \times 10^{-7} \text{ m}^{-1}$, Fig. 6b). Therefore, this subtle curvature resulting from the flexure of rigid plates is challenging to observe in the landscape because of minor variations in slope across space. Additionally, the superposition of short wavelength features created by erosion and fluvial incisions hampers the identification of these subtle curvatures. Only low T_e values ($T_e \lesssim 5$ km) were able to create perceptible plate flexure induced by short-range topographic loads with a wavelength of the order of tens of kilometers and amplitude of hundreds of meters.

Based on a global compilation of the effective elastic thickness T_e (Watts, 2001), the values for the continents range from a few kilometers to more than 100 km (Fig. 6c), with a peak around 20–25 km. High values for T_e are typically associated with stable cratonic domains, whereas low T_e values are commonly observed in rifts and other active plate boundaries. Based on this compilation, domains with T_e values under 5 km represent less than 10% of the continents. Therefore, the preservation of perceptible flexural features induced by individual fluvial incision with hundreds of meters and a wavelength of a few tens of kilometers must be an exception and only observed in regions with relatively low flexural rigidity.

6. Conclusions

Numerical thermomechanical modelling was conducted to investigate the dynamics of the lithosphere during the post-rift phase of the Recôncavo-Tucano-Jatobá basin system. A geologic-erosive profile of the Aptian sedimentary units was used as the main constraint. Based on thermo-mechanical numerical scenarios assuming different rheologies for the lithosphere and varying surface loads, we explored the feasibility of explaining the deformation of the sedimentary strata as a flexural response of the lithosphere to fluvial incisions.

Within the assumptions of the model, we find that the observed landforms are adequately reproduced in scenarios where the degree of lithospheric coupling is low and the deformational regime is characterized by strain localized mainly in crustal layers. This lithospheric decoupling may be partly due to the occurrence of magmatic underplating in the region, as suggested by Magnavita et al. (1994) and

F. Baiadori et al. Tectonophysics 877 (2024) 230292

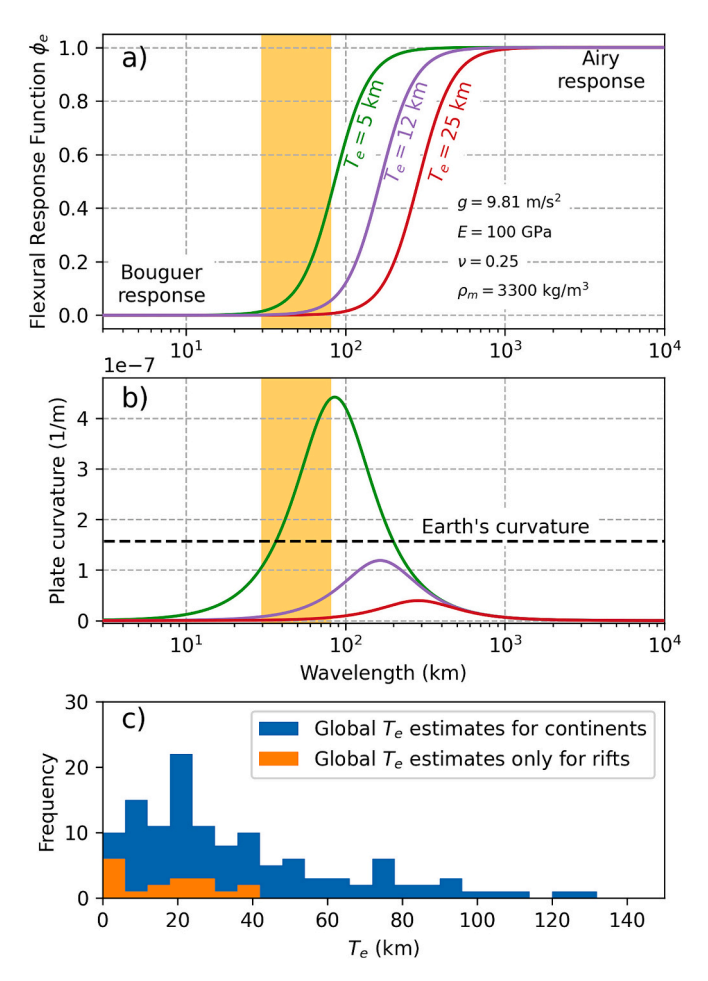


Fig. 6. a) Flexural response function ϕ_e for two different effective elastic thickness: $T_e=5$ and 25 km. The yellow stripe indicates the width range of the river valleys in the Vaza-Barris and Itapicurú Rivers. b) Plate curvature predicted for different load wavelengths, assuming a load amplitude of 200 m. The colors follow the same pattern as in (a). c) Histograms showing continental T_e estimates based on forward gravity anomaly modelling. The blue histogram indicates 125 T_e estimates for continents on different domains: foreland basins, intra-cratonic basins, rifts domains, and passive margins. The orange histogram indicates 18 T_e estimates only for rifts around the world. Values extracted from Tables 6.2 and 6.3 from Watts (2001) and references therein. (For interpretation of the references to colour in this figure legend, the reader is referred to the web version of this article.)

supported by Alvarez and Holz (2022) and Döring et al. (2022), aided by the thermal effect of the thick sedimentary package in the basin system. Furthermore, based on the equivalent thin elastic plate approach, examining the maximum curvature attained by the plate for different effective elastic thickness (T_e) values when subjected to a load representative of the sediment removal along the RTJ main river valleys indicates a T_e value of ≤ 5 km, in good agreement with the value reported by Magnavita et al. (1994).

We conclude that the expression of lithospheric bending in response to individual fluvial incisions is noticeable in the landscape only when the flexural rigidity of the lithosphere is relatively low, particularly in regions where the upper crust is partially decoupled from the lithospheric mantle.

CRediT authorship contribution statement

Felipe Baiadori: Writing – review & editing, Writing – original draft, Visualization, Software, Investigation. **Victor Sacek:** Writing – review & editing, Writing – original draft, Supervision, Software, Methodology,

Investigation, Conceptualization. **Bernardo T. Freitas:** Writing – review & editing, Validation. **Renato P. Almeida:** Writing – review & editing, Validation, Conceptualization.

Declaration of competing interest

The authors declare that they have no known competing financial interests or personal relationships that could have appeared to influence the work reported in this paper.

Data availability

Data will be made available on request.

Acknowledgements

We would like to thank two anonymous reviewers for valuable comments and suggestions that significantly improved the quality of the manuscript. The authors are thankful to CAPES for the funding provided in the form of a student scholarship (process number 88887.638901/2021-00). This work was also supported by Petrobras (process number 2022/00157-6) and CNPq (304984/2022).

References

Allen, P.A., Allen, J.R., 2013. Basin Analysis: Principles and Application to Petroleum Play Assessment. John Wiley & Sons.

Alvarez, P., Holz, M., 2022. The Tucano basin (cretaceous, Brazil)—a world-class example of an aborted rift system with anomalous depth. J. S. Am. Earth Sci. 119, 103975.
 Aragão, M., Peraro, A., 1994. Elementos estruturais do rifte Tucano/Jatobá. Simpós.
 Sobre Cretác. Brasil 3, 161–165.

Burov, E.B., Diament, M., 1995. The effective elastic thickness (T_e) of continental lithosphere: what does it really mean? J. Geophys. Res. Solid Earth 100 (B3), 3905–3927.

Gaixeta, J.M., Bueno, G.V., Magnavita, L.P., Feijó, F., 1994. Bacias do Recôncavo. Tucano e Jatobá. Boletim de Geociências da PETROBRAS, p. 8.

Costa, I., Milhomem, P., Bueno, G.V., Silva, H., Kosin, M.D., 2007. sub-bacias de tucano sul e central. Bolet. Geociênc. Petrobras 15 (2), 433–443.

Döring, M., Julià, J., Evain, M., 2022. Joint inversion of receiver functions and surface wave dispersion in the Recôncavo–Tucano basin of NE Brazil: implications for basin formation. Geophys. J. Int. 230 (1), 317–333.

Figueiredo, F.T., Almeida, R.P., Freitas, B.T., Marconato, A., Carrera, S.C., Turra, B.B., 2016. Tectonic activation, source area stratigraphy and provenance changes in a rift basin: the early cretaceous Tucano basin (NE-Brazil). Basin Res. 28 (4), 433–445.

Freitas, B.T., Almeida, R.P., Carrera, S.C., Figueiredo, F.T., Turra, B.B., Varejao, F.G., Assine, M.L., 2017. Aptian sedimentation in the Reconcavo-Tucano-Jatobá rift system and its tectonic and paleogeographic significance. J. S. Am. Earth Sci. 80, 460-481.

Garcia-Castellanos, D., 2002. Interplay between lithospheric flexure and river transport in foreland basins. Basin Res. 14 (2), 89–104.

Gilchrist, A., Summerfield, M., 1990. Differential denudation and flexural isostasy in formation of rifted-margin upwarps. Nature 346 (6286), 739–742.

Gleason, G.C., Tullis, J., 1995. A flow law for dislocation creep of quartz aggregates determined with the molten salt cell. Tectonophysics 247 (1–4), 1–23.

Gomes, C.P.J., Fossen, H., Almeida, R.P., Salmoni, B., 2018. Subseismic deformation in the Vaza-Barris transfer zone in the cretaceous Reconcavo-Tucano-Jatobá rift system, NE Brazil. J. Struct. Geol. 117, 81–95.

Gordon, A., Destro, N., Heilbron, M., 2017. The Recôncavo-Tucano-Jatobá Rift and Associated Atlantic Continental Margin Basins. Tectonic Genealogy of a Miniature Continent, São Francisco Craton, Eastern Brazil, pp. 171–185.

Haq, B.U., 2014. Cretaceous eustasy revisited. Glob. Planet. Chang. 113, 44–58.
 Karato, S.-I., Wu, P., 1993. Rheology of the upper mantle: a synthesis. Science 260 (5109), 771–778.

Kooi, H., Beaumont, C., 1994. Escarpment evolution on high-elevation rifted margins: insights derived from a surface processes model that combines diffusion, advection, and reaction. J. Geophys. Res. Solid Earth 99 (B6), 12191–12209.

Lavier, L.L., Steckler, M.S., 1997. The effect of sedimentary cover on the flexural strength of continental lithosphere. Nature 389 (6650), 476–479.

MacFerrin, M.J., Amante, C., Carignan, K., Love, M.R., Lim, E., Arcos, N.P., Stroker, K.J., 2022. ETOPO 2022: NOAA's new seamless topography-and-bathymetry bare earth surface elevation dataset. In: AGU Fall Meeting Abstracts, 2022. NH22C-0433.

Magnavita, L.P., Cupertino, J.A., 1988. A new approach to the geological configuration of the lower cretaceous Tucano and Jatobá basins, northeastern Brazil. Rev. Brasil. Geociênc. 18 (2), 222–230.

Magnavita, L.P., Davison, I., Kusznir, N.J., 1994. Rifting, erosion, and uplift history of the Reconcavo-Tucano-Jatobá Rift, Northeast Brazil. Tectonics 13 (2), 367–388.

Matos, R.M.D., 1992. The northeast Brazilian rift system. Tectonics 11 (4), 766–791.

- Milani, E.J., Davison, I., 1988. Basement control and transfer tectonics in the Recôncavo-Tucano-Jatobá rift, Northeast Brazil. Tectonophysics 154 (1–2), 41–70.
- Montgomery, D.R., Stolar, D.B., 2006. Reconsidering Himalayan river anticlines. Geomorphology 82 (1–2), 4–15.
- Moresi, L., Solomatov, V., 1998. Mantle convection with a brittle lithosphere: thoughts on the global tectonic styles of the earth and venus. Geophys. J. Int. 133 (3), 669–682.
- Neumann, V.H., Rocha, D.E., 2014. Stratigraphy of the post-rift sequences of the Jatobá basin, northeastern Brazil. In: STRATI 2013: First International Congress on Stratigraphy at the Cutting Edge of Stratigraphy. Springer, pp. 553–557.
- Oliveira, A.L.S., de Lira Santos, L.C.M., Tedeschi, M., Queiroga, G., Viegas, G., Cawood, P.A., 2023. On the crustal framework of the central alto pajeú terrane (Borborema province, ne Brazil): geophysical and structural data constrain late neoproterozoic transpression in western gondwana. Tectonophysics 854, 229811.
- Sacek, V., 2017. Post-rift influence of small-scale convection on the landscape evolution at divergent continental margins. Earth Planet. Sci. Lett. 459, 48–57.
- Sacek, V., Assunção, J., Pesce, A., da Silva, R.M., 2022. Mandyoc: a finite element code to simulate thermochemical convection in parallel. J. Open Sour. Softw. 7 (71), 4070.
- Salazar-Mora, C.A., Sacek, V., 2023. Effects of tectonic quiescence between orogeny and rifting. Tectonics 42 (2), e2022TC007492.

- Silva, R.M., Sacek, V., 2022. Influence of surface processes on postrift faulting during divergent margins evolution. Tectonics 41 (2), e2021TC006808.
- Silva, O.B., Caixeta, J., Milhomem, P., Kosin, M.D., 2007. Bacia do recôncavo. Boletim Geociênc. Petrob. 15 (2), 423–431.
- Silva, J.P.M., Sacek, V., da Silva, R.M., 2023. The influence of lithospheric rheology and surface processes on the preservation of escarpments at rifted margins. Tectonophysics 851, 229769.
- Simpson, G., 2004. Role of river incision in enhancing deformation. Geology 32 (4), 341–344.
- Tucker, G.E., Slingerland, R.L., 1994. Erosional dynamics, flexural isostasy, and long-lived escarpments: a numerical modeling study. J. Geophys. Res. Solid Earth 99 (B6), 12229–12243.
- Turcotte, D.L., Schubert, G., 2002. Geodynamics. Cambridge University Press.
- Varejão, F.G., Warren, L.V., de Jesus Perinotto, J.A., Neumann, V.H., Freitas, B.T., Almeida, R.P., Assine, M.L., 2016. Upper aptian mixed carbonate-siliciclastic sequences from Tucano Basin, Northeastern Brazil: implications for paleogeographic reconstructions following gondwana break-up. Cretac. Res. 67, 44–58.
- Watts, A.B., 2001. Isostasy and Flexure of the Lithosphere. Cambridge University Press.